Available online at www.sciencedirect.com
ScienceDirect
Journal of the European Ceramic Society 30 (2010) 1527–1535
www.elsevier.com/locate/jeurceramsoc

Microstructural development of a C_f/ZrC composite manufactured by reactive melt infiltration

Linhua Zou [a,*], Natalie Wali [a], Jenn-Ming Yang [a], Narottam P. Bansal [b]

[a] *Department of Materials Science and Engineering, University of California, Los Angeles, CA 90095-1595, USA*
[b] *NASA Glenn Research Center, Cleveland, OH 44135, USA*

Received 9 April 2009; received in revised form 30 September 2009; accepted 20 October 2009
Available online 8 December 2009

Abstract

The microstructural development of a carbon fibre reinforced ZrC matrix composite, C_f/ZrC, manufactured by reactive melt infiltration (RMI) was investigated. The microstructural features of the composite were revealed by optical microscopy (OM), X-ray diffraction (XRD), scanning electron microscopy (SEM), and transmission electron microscopy (TEM). It was found that the carbon fibre bundles are surrounded by continuous ZrC layers, while the composite matrix is composed of island-like ZrC particles dispersed within an α-Zr–ZrC eutectic phase. Nanosized inclusions were found inside some ZrC particles and it was demonstrated that they were α-Zr or α-Zr–ZrC. A formation mechanism of the unique matrix microstructure is proposed.

Keywords: Composites (B); Microstructure (B); Carbon (D); ZrC; Reactive melt infiltration

1. Introduction

New and innovative structural materials capable of prolonged operation in oxidizing environments at temperatures above 2000 °C are required for future space systems.[1] For example, sharp leading edges and nose tips of advanced hypersonic and space vehicles will have to withstand exposure to high temperatures (>2200 °C) and severe thermal cycling in both neutral and oxidizing environments. The combustion temperature of a liquid bipropellant rocket engine used for placing satellites in orbit and planetary exploration will reach close to 3000 °C. The extreme operational conditions encountered for hypersonic and space vehicles as well as rocket propulsion systems present a great challenge to the development of ultra high temperature materials.

The most widely studied ultra high temperature materials (UHTMs) are refractory borides, nitrides and carbides. Among these ultrahigh temperature ceramics, ZrC possesses a melting point as high as 3540 °C and is one of the most promising candidates for ultra-high temperature applications due to the 2700 °C (∼4900 °F) melting point of its protective zirconia (ZrO_2) layer. The oxidation resistance of ZrC is comparable to that of hafnium carbide, HfC, and the density of ZrC (6.73 g/cm^3) is about half that of HfC (12.2 g/cm^3). However, ZrC ceramics are brittle and display little to no plasticity within a broad temperature range. As a result, the incorporation of fibres is needed to improve the fracture resistance and damage tolerance of ZrC. Various approaches such as chemical vapor infiltration (CVI), hot pressing, spark plasma sintering (SPS), RMI, etc. can be used to fabricate fibre-reinforced ZrC composites. CVI is a lengthy and expensive manufacturing process for ceramic matrix composites (CMCs). Additionally, it is very difficult to fabricate a fully dense CMC. Hot pressing or SPS of fibre/powder stacks is another technique for consolidating ZrC-based composites. However, both hot pressing and SPS are also extremely costly due to the high pressures and temperatures involved, and it is virtually impossible to fabricate complex geometries using these techniques. As a result, both CVI and hot pressing/SPS are not practical manufacturing processes for ZrC-based composites. Because of these challenges, limited efforts have been made to develop a ZrC-based composite for ultrahigh temperature aero-structures.

Reactive melt infiltration/reaction (RMI) has been demonstrated as a rapid and low-cost manufacturing process

* Corresponding author. Tel.: +1 310 825 2758; fax: +1 310 206 7353.
E-mail address: linhua_zou@hotmail.edu (L. Zou).

0955-2219/$ – see front matter © 2009 Published by Elsevier Ltd.
doi:10.1016/j.jeurceramsoc.2009.10.016

for structural components made of carbon/silicon carbide composites.[2–7] However, carbon/zirconium carbide composites fabricated by RMI still have not been reported so far. RMI can be used when one of the ceramic matrix elements possesses a relatively low melting point and readily wets the fibres. Ideally, in RMI all available macroscopic porosities (i.e. the porosity between fibre laminates and tows) are rapidly filled to yield a dense, uniformly infiltrated composite. Furthermore, components with complex geometries, such as sharp leading edges and rocket engine combustion chambers, can be fabricated easily by RMI.

In this study, the microstructural development of a C_f/ZrC composite manufactured by RMI was studied based on microstructural analysis, with focus especially on the matrix. A microstructural formation mechanism is proposed.

2. Experimental

2.1. Materials

The carbon fibre reinforced ZrC composite was fabricated by Ultramet (Pacoima, CA, USA) using RMI. A high strength carbon fibre, T700S (Toray, Japan) was selected. In the first processing step, a carbon fibre preform was coated with the desired interface. The coated fibres were then woven into a two-dimensional fabric preform. Next, a controlled level of carbon was rapidly deposited onto the preform using CVD to form a porous C/C skeleton. Molten zirconium then infiltrated the porous preform by wicking action. The molten metal was drawn along the carbon fibre tows by capillary forces, where it reacted with the previously deposited carbon to form the ZrC matrix.

2.2. Microstructural characterization

The microstructural features of the melt infiltrated composite were thoroughly analyzed using various techniques, including X-ray diffraction (XRD), scanning electron microscopy (SEM) and transmission electron microscopy (TEM).

Optical images were taken using a Nikon 9600 light optical microscope with Q Capture software for image acquisition. Cross-sectional view and top view samples were polished to 0.05 μm for observation. Sample etching was performed with a Unaxis SLR770 ICP Minispec system in flowing Cl_2. The recipe adopted contained 50 vol% BCl_3, 10 vol% Ar, and 40 vol% Cl_2.

A Panalytical X'Pert Pro X-ray Powder Diffractometer was used to carry out X-ray diffraction analysis using a Cu target. Voltage was set as 45 kV, current 40 mA, and a X'celerator RTMS Scanning Detector was used. X'pert highscore software was used to identify each peak.

SEM images were obtained with a LEO 1550VP FE-SEM with Smart SEM software. EDAX was performed using INCA software for the LEO 1550VP to determine chemical composition.

Several TEM samples from within ZrC particles were prepared by a focused ion beam (FIB). Conventional methods were also used to prepare matrix area samples. TEM samples were prepared by grinding a bulk sample to ~50 μm in thickness and then a 3 mm diameter disc was cut out. The disc was subsequently dimpled and ion milled. Images and selected area electron diffraction (SAED) patterns were obtained with a JEOL 100CX and a FEI PHILIPS-CM300 TEM.

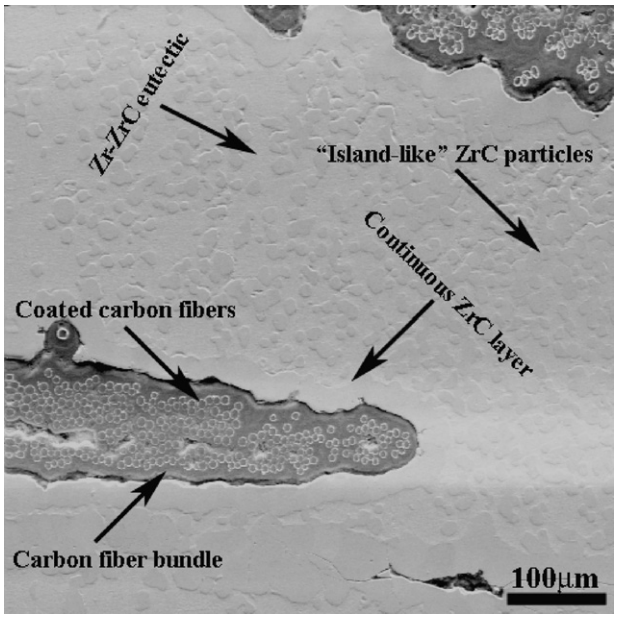

Fig. 1. SEM micrograph of the polished cross section surface of the C_f/ZrC composite with labeled microstructural sites of interest.

3. Results

3.1. General microstructural features of the C_f/ZrC composite

Microstructural characterization was conducted to analyze the different phases of the C_f/ZrC composite. The work included studying phase morphologies and determining the overall formation mechanism of the microstructure. A representative area

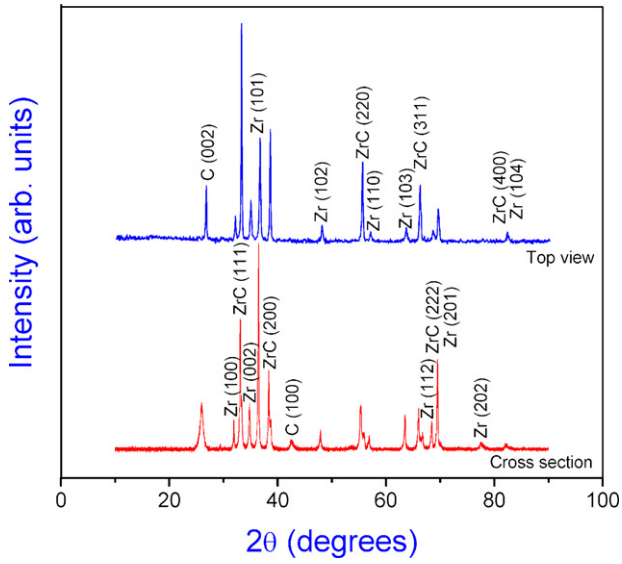

Fig. 2. XRD pattern of the C_f/ZrC composite.

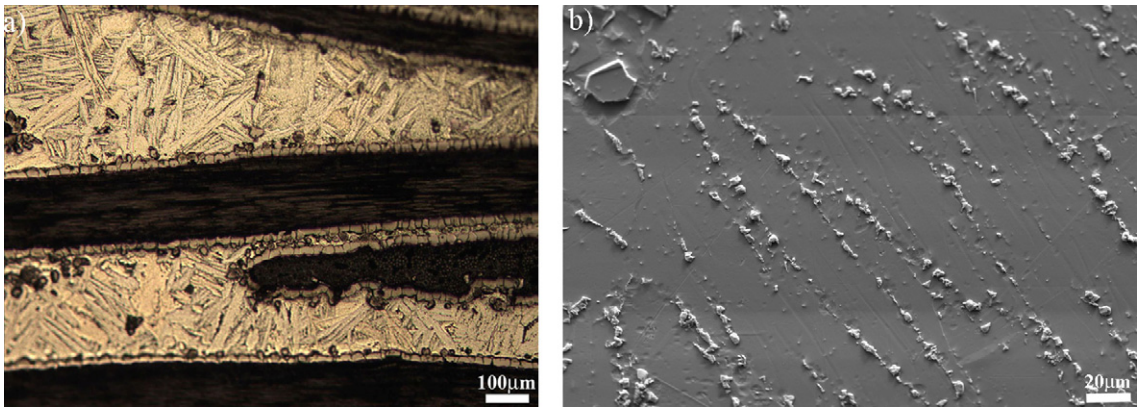

Fig. 3. Micrographs of the eutectic phase in the C_f/ZrC composite after plasma etching for 8 min. (a) Optical micrograph and (b) SEM secondary electron image.

of the composite is shown in Fig. 1. Shown are carbon fibre bundles surrounded by continuous layers, the fibre coatings that had been deposited before processing, and island-like particles distributed throughout a continuous phase in the matrix. X-ray diffraction results (Fig. 2) of both cross-sectional and top-view samples show that there exist three phases in the C_f/ZrC composite: carbon, zirconium carbide and alpha zirconium, where the zirconium phase is residual Zr metal.

The formation of the eutectic phase is confirmed by microscopy studies. As shown in Fig. 3, both optical microscope and SEM micrographs indicate that the continuous matrix phase among ZrC particles possesses a layered structure characteristic of a eutectic. XRD patterns and EDAX analysis further confirmed that this was the Zr–ZrC eutectic phase, while both the "island-like" particles and the continuous layers around the carbon fibre bundles were identified as ZrC (Fig. 4). In addition to Zr and C peaks, the EDAX analysis also detected the presence of the elements B, O and Al, which are most likely due to sample preparation. SEM analysis also revealed the presence of many small white features inside some ZrC grains. More studies were carried out on a fully plasma etched sample to characterize the inner microstructure of some of these interesting ZrC grains.

Analysis of the plasma etched sample shows that these interesting features possess unique morphologies. The microstructure of the ZrC grains before and after plasma etching shows that these white inclusions are easily etched away, leaving pores in their place (Fig. 5b). The inclusions are ellipsoidal with nano-scale diameters and large aspect ratios. After etching the depressions left behind are large holes with microscopically rough surfaces (Fig. 5a). These inclusions merited further study.

3.2. TEM studies of ZrC particles in the composite matrix

TEM analysis was conducted on a sample prepared from a ZrC particle about 20 μm across, containing inclusions of both ellipsoidal and needle-like shapes (Fig. 6a). A bright-field image

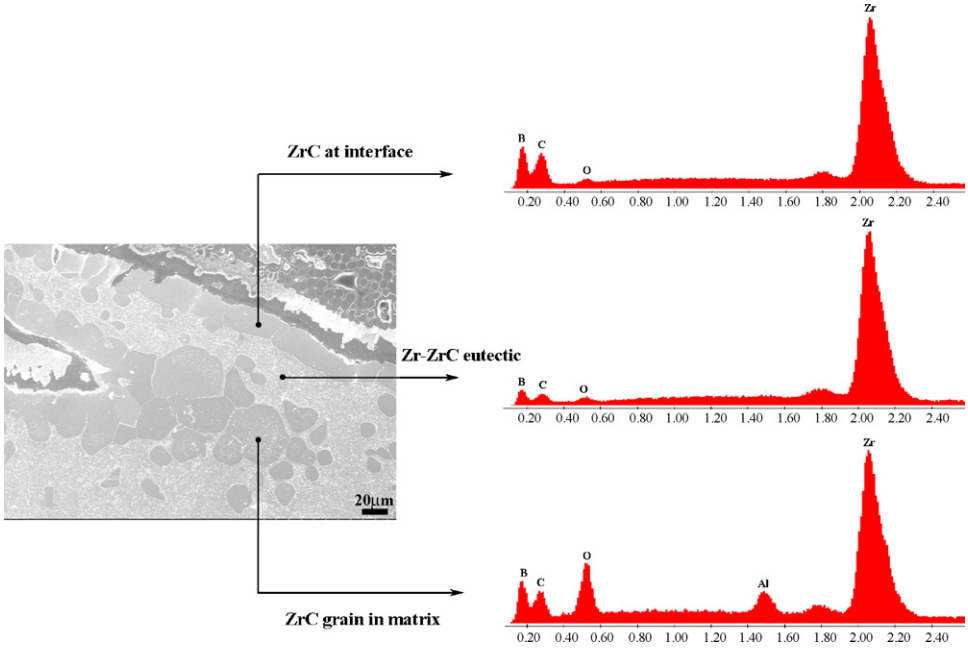

Fig. 4. The SEM micrographs with corresponding EDAX analysis on different phases in the C_f/ZrC composite after plasma etching for 30 s.

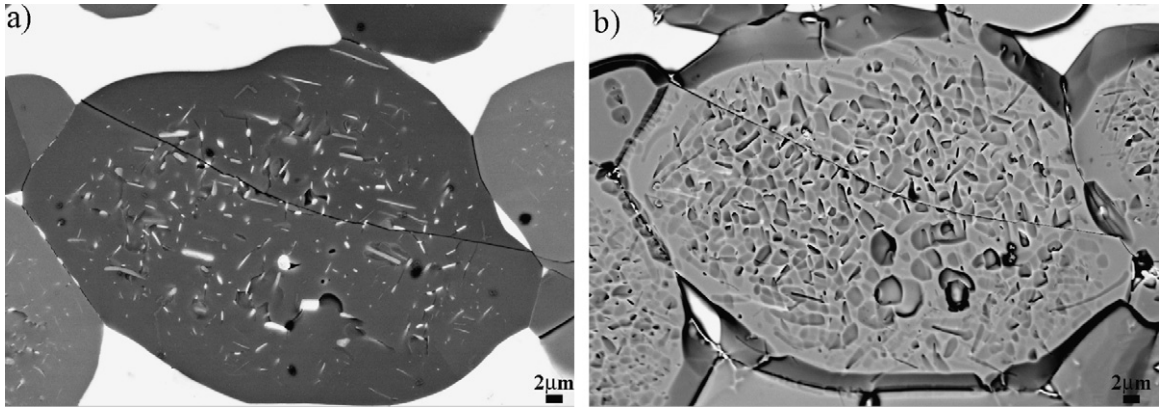

Fig. 5. The SEM micrographs of the C_f/ZrC composite surface (top-view sample) before and after etching (8 min). (a) Microstructure before etching and (b) microstructure after etching.

was taken of the specimen and it shows that the inclusions are rather sparsely distributed within the ZrC matrix (Fig. 6b). Selected area electron diffraction (SAED) performed on the circled area confirms that the sample is a single crystal of ZrC (Fig. 6b, inset). An SAED pattern taken of the inclusion (Fig. 6c) contains low order diffractions of both ZrC and α-Zr (Fig. 6d). This indicates that the inclusion is composed of the eutectic Zr–ZrC phase.

Another large ZrC particle was prepared for TEM study. The SAED taken of the central area in Fig. 7a is a spot pattern overlaid with rings, which indicates polycrystallinity (Fig. 7b). Both patterns were found to be characteristic of ZrC.

Not all ZrC particles in the composite matrix are micron-sized like the one in Fig. 6. A nano-sized ZrC grain was examined by TEM (Fig. 8) and also found to be a single crystal. The diffraction results of the samples shown in Figs. 6–8 demonstrate that the particles in the matrix are either single- or polycrystalline ZrC.

A high resolution TEM image (Fig. 9) was taken of the interface between two small ZrC grains. The (1 1 1) planes of the two

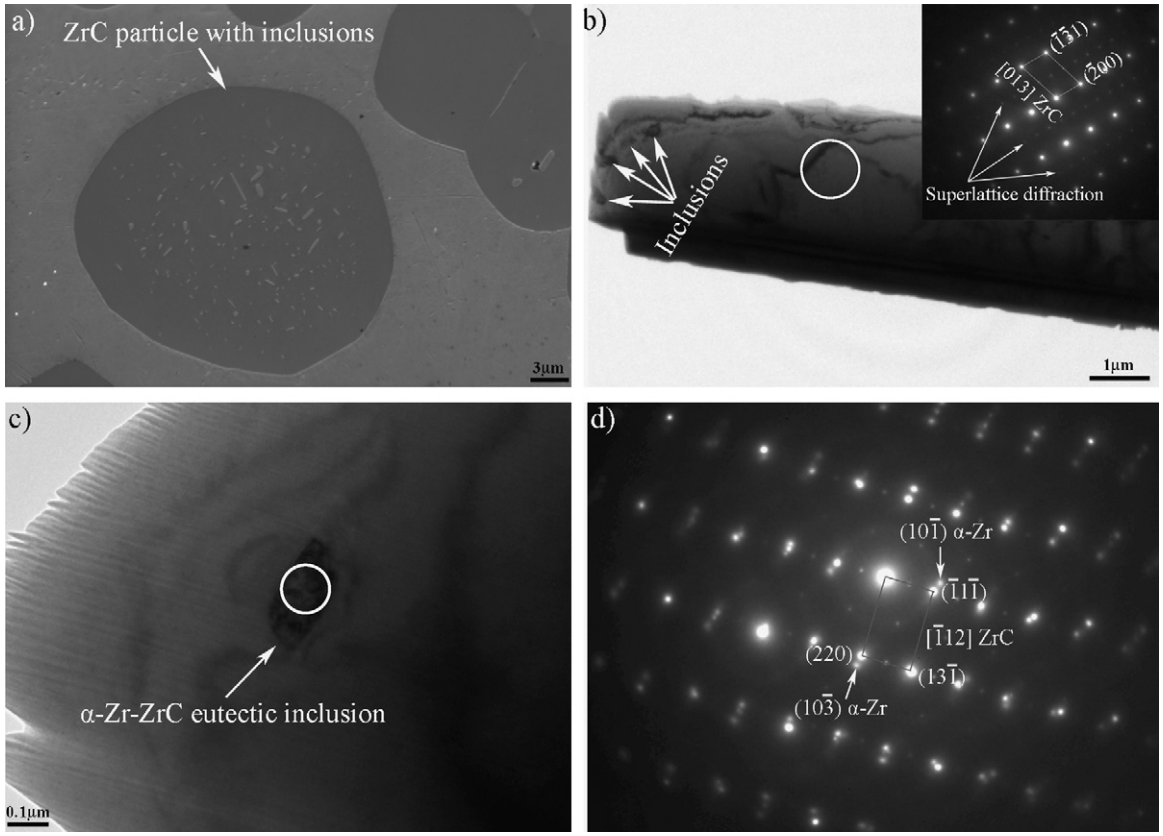

Fig. 6. Micrographs and SAED patterns showing inclusions inside a ZrC grain: (a) SEM image showing a ZrC particle with spot or "needle-like" tiny inclusions; (b) BF image of the ZrC particle with a inset showing the diffraction pattern of the circled area; (c) BF image showing an inclusion within the ZrC particle and (d) the diffraction pattern from the inclusion.

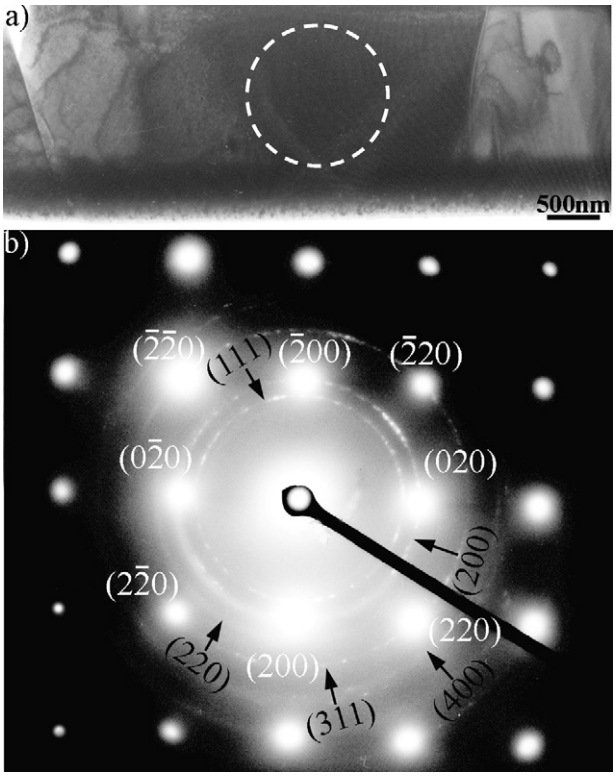

Fig. 7. TEM image and diffraction pattern showing: (a) bright-field image of an "island-like" ZrC particle, (b) diffraction patterns from fundamental f.c.c. ZrC single crystal and polycrystalline. For diffraction of fundamental f.c.c, zone axis: [0 0 1].

crystals are oriented at 23° relative to each other. The locations of several nanosized α-Zr inclusions are indicated by arrows.

The results presented in Figs. 6 and 9 demonstrate that the inclusions are composed of either the α-Zr or α-Zr–ZrC eutectic phase. Knowing this phase information is the first step to

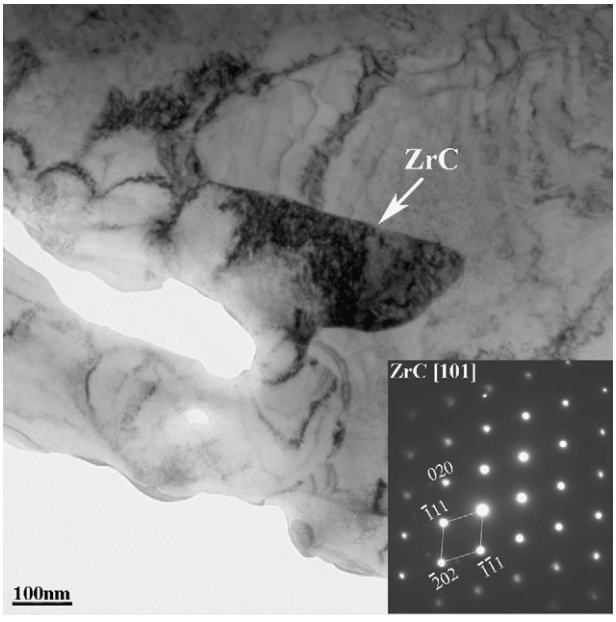

Fig. 8. TEM BF image showing a ZrC crystal in the matrix of the C_f/ZrC composite (the inset showing the diffraction pattern from the ZrC crystal).

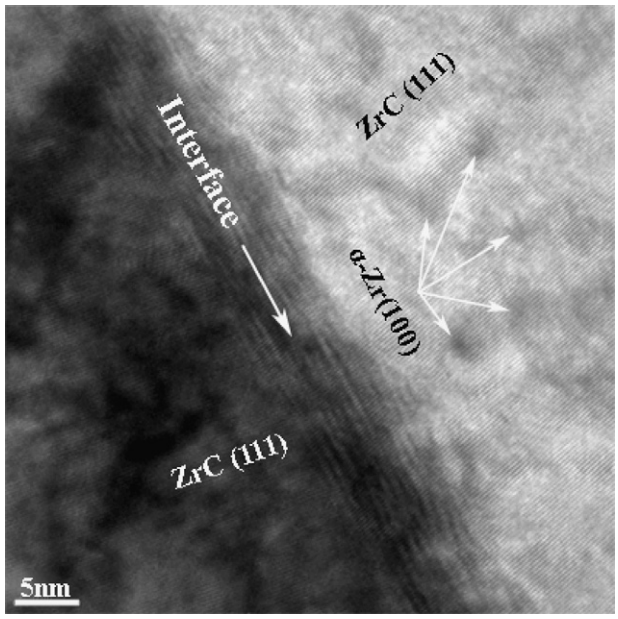

Fig. 9. HRTEM image showing nanosized α-Zr inclusions inside ZrC crystal.

providing an explanation of their presence inside some ZrC particles and not others. The details are presented in the following microstructure formation mechanism.

4. Discussion

Ceramic matrix composites produced by reactive melt infiltration possess a multiphase and heterogeneous matrix microstructure. The desired outcome of RMI is to produce a composite with as much of the ceramic phase as possible. To better understand the microstructure development of the C_f/ZrC matrix, C/SiC produced by reactive melt infiltration is discussed as for comparison. From the phase diagram of the Si–C system,[8] shown in Fig. 10, it can be seen that the phase region is β-SiC when the carbon concentration in the silicon melt is higher than 50 at.%. When the carbon concentration is below 50 at.%, the system will be in the two-phase region, which is liquid and β-SiC. SiC precipitates with the temperature decrease, until finally, the eutectic phase Si–SiC is formed when the temperature reaches 1404 °C. Though a well-studied system, there is still much disagreement regarding the formation of SiC during RMI. The two differing mechanisms reported in the literature maintain that either (1) formation of SiC is limited by the diffusivity of carbon and Si through SiC (Fitzer and Gadow[9] and Li and Hausner[10]); or that (2) formation of SiC proceeds by a solution-precipitation process (Pampuch et al.,[11] Ness and Page,[12] and Singh and Behrendt[13]).

In the first mechanism, Fitzer and Gadow[9] and Li and Hausner[10] suggest a two stage mechanism. First, the heterogeneous nucleation and growth of SiC leads to the formation of a continuous polycrystalline SiC layer. Further growth of the layer is attributed to the diffusion of the reactive species through the silicon carbide coating. According to Li and Hausner,[10] growth of the SiC layer at the carbon source occurs through carbon dissolution in liquid silicon. This dissolution process

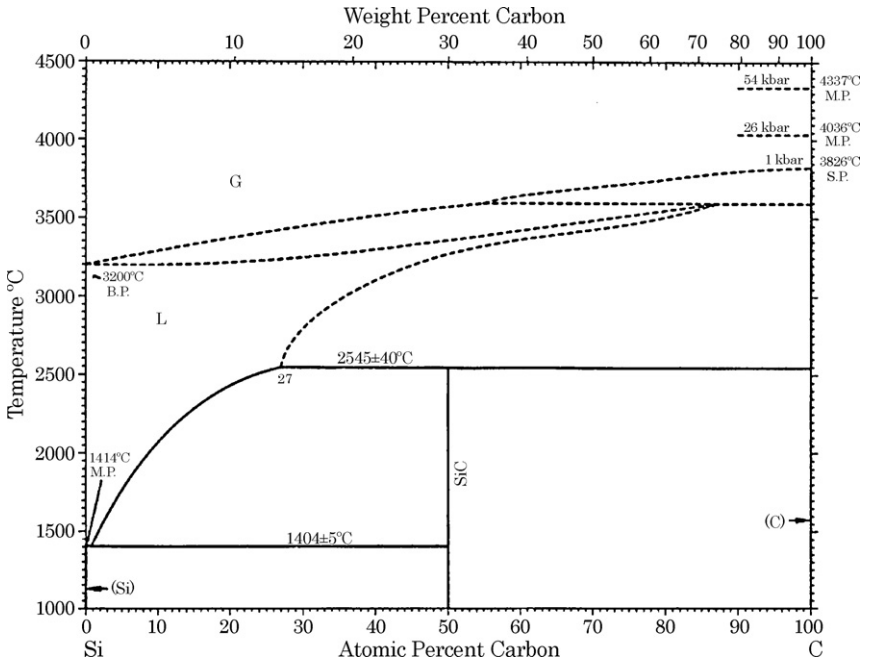

Fig. 10. Si–C phase diagram.[8]

forms Si–C clusters that adsorb onto the liquid/solid interface. After saturation of this adsorption layer by the Si–C clusters, a two-dimensional continuous SiC layer forms through a heterogeneous nucleation and crystal growth process. The formation of this initial continuous SiC layer is very fast, and the subsequent growth is controlled by diffusion of C through the SiC layer. In the second mechanism, carbon dissolves into the silicon melt and then SiC precipitates from the supersaturated solution. The carbon dissolution in Si is exothermic, so the entrance of some carbon into the melt causes a local temperature increase which in turn causes more carbon to dissolve. The temperature gradient in the liquid Si spurs rapid carbon diffusion into the melt to cooler sites where it then precipitates as SiC.

Favre also reported on the microstructure and mechanism of reaction-bonded SiC.[14] An important feature of their material that also appeared in the matrix of the C_f/ZrC composite was the presence of isolated carbide crystallites in the metal phase. This was attributed by Favre to the break-up of the SiC layer and scattering of isolated SiC particles into the Si matrix. The authors determined that the growth of the SiC particles occurred by a crystallization and fragmentation mechanism.

The similarity of binary phase diagrams of Si–C and Zr–C systems (Figs. 10 and 11) implies that the mechanism of reactive melt infiltration for the two systems might be similar theoretically. In both systems, after the continuous carbide layer is produced, further production of carbide depends on carbon diffusion through the carbide layer into the isolated molten metal. Due to the limitation of carbon solubility in the liquid metal, the composition falls in the two-phase region, where liquid metal and carbide coexist. When the temperature drops, the carbide will precipitate from the carbon-saturated metal solution until the eutectic temperature. At point, all the metal liquid transforms into the eutectic phase. However, as the temperature continues to drop the phase transformation of β-Zr → α-Zr occurs at 865 °C in the Zr–C system.[15] In addition, the C solubility in Zr at the eutectic temperature (∼1.0 at.%) is much higher than that of C in Si (1.8×10^{-4} at.%).[8,16] Only when the carbon concentration increases to ∼38.5 at.%, can ZrC form through the reaction between Zr and C, however, for the Si–C system, SiC forms through the reaction between C and Si only when the carbon concentration reaches 50 at.%. According to the lever law, the mass ratio of residual silicon to silicon carbide in the eutectic is much larger than that of residual zirconium to zirconium carbide in Zr–ZrC.

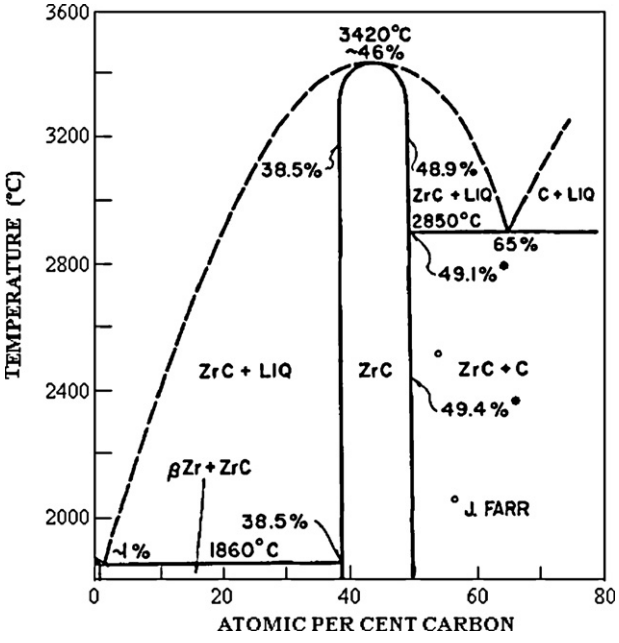

Fig. 11. Zr–C binary phase diagram.[17]

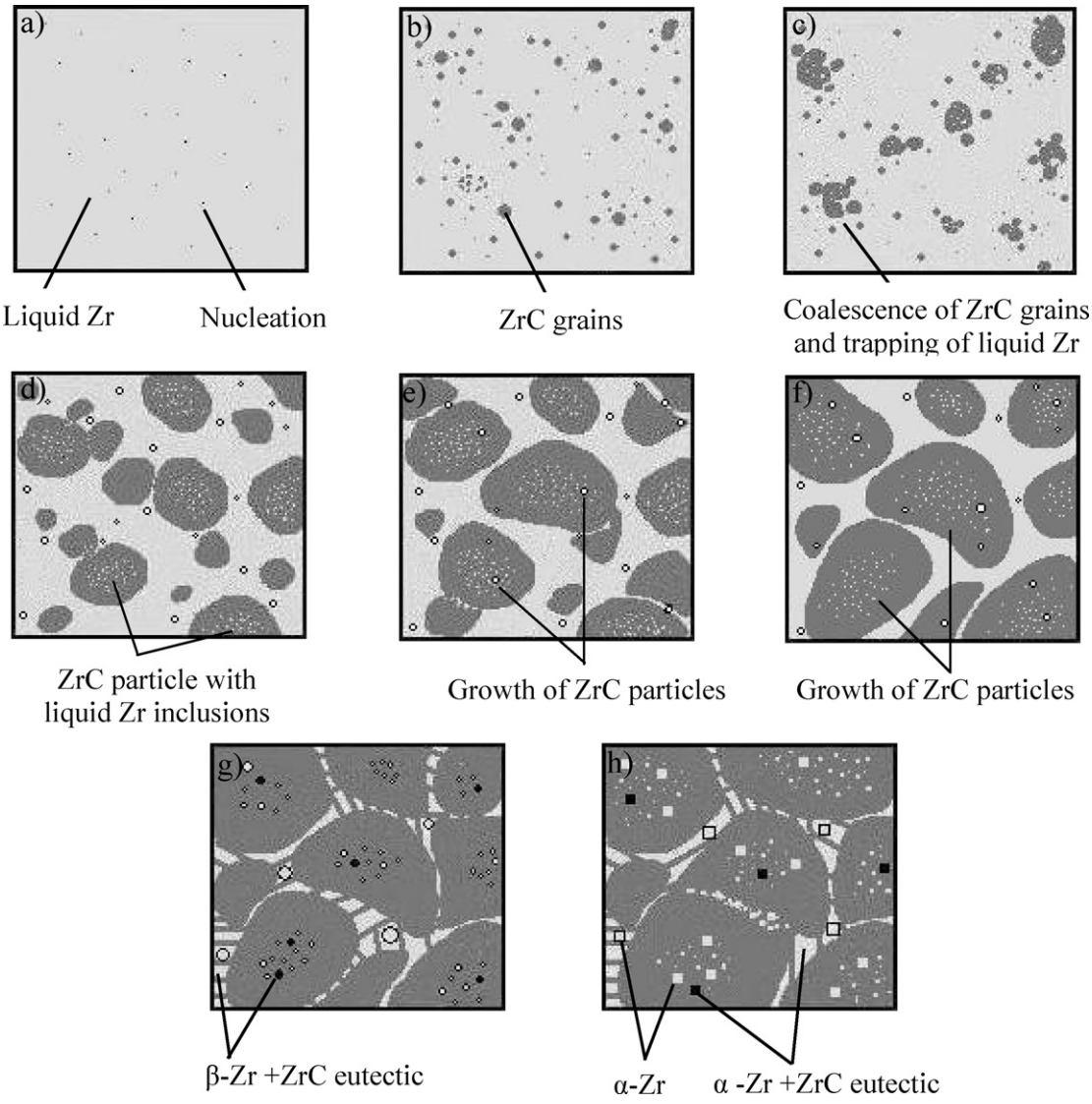

Fig. 12. Schematic of the matrix microstructure formation mechanism of the C_f/ZrC composite. (a) Heterogeneous nucleation sites of ZrC at 1950 °C; (b) growth and grouping of ZrC grains at 1950 °C; (c) coalescence of ZrC grains and trapping of liquid Zr at 1950 °C; (d) growth of ZrC particles with liquid Zr inclusions and precipitation of β-Zr at 1950 °C; (e) coalescence, growth of ZrC, and trapping of β-Zr as temperature decreases (above 1835 °C); (f) transformation of liquid Zr into the eutectic phase at 1835 °C; (g) phase transformation of β-Zr into α-Zr at 1159 °C and (h) final microstructure at room temperature, showing ZrC particles with α-Zr + ZrC and α-Zr inclusions. The eutectic phase composed of α-Zr + ZrC and α-Zr serves as the grain boundaries in areas of densely distributed ZrC particles.

In an earlier work by Adelsberg et al.,[16] the kinetics of the zirconium–carbon reaction at temperatures above 2000 °C were studied, the thickness of the continuous ZrC layer as a function of time and temperature was obtained, at each temperature investigated from 2000 °C to 2860 °C. The results showed that the ZrC phase grew parabolically into the carbon-saturated liquid, which is indicative of diffusion-controlled reaction. It was demonstrated that this was controlled by carbon diffusion through the ZrC. The carbon solubilities were also measured. The results indicated that the carbon solubilities were independent of the reaction times. The metallographic examination showed that the ZrC precipitates were found in the metal upon cooling and distributed uniformly throughout the frozen metal matrix.

Based on our characterization results, Adelsberg et al.'s work,[16] and the Zr–C phase diagram in Fig. 11,[17] the following matrix microstructural formation mechanism of the C_f/ZrC composite is proposed. At the beginning of RMI, the processing temperature was set above the 1875 °C Zr melting point. A continuous product layer formed when the infiltrating zirconium metal came into contact with the pyrolytic carbon layer in the preform and reacted to form ZrC. As the ZrC layer grew it separated the remaining molten Zr from the pyrolytic carbon layer. Any subsequent reactions occurred at the metal-carbide interface by carbon diffusion through the ZrC layer, i.e. the rate-determining step of the reaction.[16] Due to this diffusion, the carbon concentration in the molten zirconium was below 38.5 at.% based on Zr–C binary phase diagram system.[17] According to Adelsberg et al.,[16] the solubility limit of carbon in liquid zirconium is 1.36 at.% at 2000 °C, so the infiltration temperature for this process was set to guarantee that the carbon concentration in the melt fell above 1.0 at.%, which corresponds to temperatures above ~1860 °C. Coupling this with knowl-

edge of the phase diagram, the carbon concentration falls within the range of 1.0–38.5 at.%, in the liquid zirconium and zirconium carbide phase region. In the melt, however, the carbon concentration is much less, e.g. about ~8.5 at.% at 2500 °C.[16]

The start of the reaction process occurred as the temperature was held at the infiltration temperature, but some temperatures fluctuations were unavoidable. This contributed to the creation of heterogeneous nucleation sites. ZrC nucleated at these sites during the initial undercooling, along with continued growth of ZrC at the Zr–ZrC interface. This process is illustrated by the schematic in Fig. 12. During temperature holding and the initial undercooling stages, some tiny ZrC particles were produced at heterogeneous nucleation sites. As some ZrC grains grew at the Zr–ZrC interface, others coalesced into larger particles (Fig. 12b). In some instances, liquid zirconium became trapped inside a large ZrC grain during the process of coalescence (Fig. 12c and d). The growth of ZrC grains was accompanied by a corresponding decrease in the amount of zirconium melt (Fig. 12e and f). These processes, coupled with ongoing carbon diffusion, continued until the end of infiltration and a decrease in temperature to below the initial holding temperature but above the eutectic point of 1835 °C.

During cool down, reaction, growth and coalescence continued at a slower rate. ZrC continued to precipitate from the liquid Zr, and subsequently, more ZrC particles were produced until 1835 °C.

At 1835 °C, the eutectic reaction occurred. All liquid zirconium, including that trapped inside ZrC particles, transformed into the β-Zr–ZrC eutectic phase (Fig. 12g). With further cooling, most of the reaction and growth processes slowed further, and some stopped completely.

Below 865 °C, all of the β-Zr + ZrC eutectic was transformed into the α-Zr + ZrC eutectic[18] (Fig. 12g). As shown in Fig. 12g and h, the inclusions composed of the eutectic inside the ZrC particles became α-Zr + ZrC and the grain boundaries of the ZrC particles transformed into α-Zr + ZrC.

TEM studies had determined that some of the inclusions are composed of α-Zr and not the eutectic. It is surmised that some of the ZrC in the eutectic gets incorporated into the surrounding matrix of the ZrC grain so that only α-Zr is left. Further studies are needed to confirm this.

The shape of an inclusion or precipitate is largely influenced by the elastic strain energy. According to Nabarro,[19] the elastic strain energy for a homogeneous incompressible inclusion in an isotropic matrix can be expressed as:

$$\Delta G_s = \frac{2}{3}\mu\,\Delta^2 V f\left(\frac{c}{a}\right) \quad (1)$$

where μ is the shear modulus of the matrix, Δ is the volume misfit and V is the volume of the unconstrained hole in the matrix. The function $f(c/a)$ is a factor that takes into account shape effects. For a given volume, a sphere ($c/a = 1$) has the highest misfit strain energy while a thin, oblate spheroid ($c/a \to 0$) has a very low misfit strain energy, and a needle shape ($c/a = \infty$) is in the middle range of both.[20] Therefore, according to Nabarro's approximation, the equilibrium shape of an inclusion should be an oblate spheroid. The α-Zr–ZrC inclusions observed in the C_f/ZrC composite have either a spheroidal shape or a needle shape (Fig. 5), which agrees well with the idea of misfit strains.

5. Conclusions

The microstructural development of a C_f/ZrC composite manufactured by RMI processing was investigated by different characterization techniques. The results demonstrated the existence of three phases: carbon, zirconium carbide and α-zirconium. The island-like particles in the matrix were found to be either single- or polycrystalline ZrC. The continuous matrix phase around these ZrC particles was found to be composed of the eutectic phase α-Zr + ZrC. Nanosized α-Zr and/or α-Zr–ZrC eutectic inclusions were detected inside some ZrC crystals in the matrix. Analysis determined that during the holding and initial cooling stages of reactive melt infiltration, some ZrC nuclei were produced and grew into small grains which grew larger through coalescence.

A formation mechanism of the matrix microstructure was also proposed. ZrC growth was diffusion controlled and determined by the diffusivity of carbon through the growing ZrC product layer around the carbon source. During temperature holding and initial undercooling stages, heterogeneous nucleation of small ZrC particles occurred. Some of these particles grew coalesced to form larger island-like ZrC particles dispersed in the melt. As some particles coalesced they trapped liquid zirconium inside as inclusions. At the eutectic temperature all residual liquid zirconium was transformed into the eutectic β-Zr + ZrC phase. This was followed by the β-Zr → α-Zr phase transformation at still lower temperatures. The final inclusions are composed of either α-Zr or α-Zr–ZrC.

Acknowledgements

The authors acknowledge Dr. Fran Hurwitz at NASA Glenn Research Center for his support and guidance on this project and Dr. Arthur Allen at Ultramet for his contribution to the processing. The authors would also like to thank Dr. Chi Ma at the California Institute of Technology for help in SEM characterization, Dr. Sergey Prikhodko at the University of California Los Angeles for his aid in TEM characterization, Dr. Dong Yan at the University of California Riverside for TEM sample preparation by Focused Ion Beam, and Dr. Krassimir N. Bozhilov at the University of California Riverside for his help in TEM characterization.

References

1. Fahrenholtz WG, Hilmas GE. *UHTM Workshop Draft Report NSF-AFOSR Joint Workshop on Future Ultra-High Temperature Materials*. 2004.
2. Krenkel W. Carbon fibre reinforced ceramic matrix composites for high performance structures. *Int J Appl Ceram Technol* 2004;**1**:188–200.
3. Hillig WB. Melt infiltration approach to ceramic matrix composites. *J Am Ceram Soc* 1988;**71**:C-96–9.
4. Messner RP, Chiang Y-M. Liquid-phase reaction-bonding of silicon carbide using alloyed silicon–molybdenum melts. *J Am Ceram Soc* 1990;**73**:1193–200.

5. Chakrabarti O, Das PK. Reactive Infiltration of Si–Mo alloyed melt into carbonaceous preforms of silicon carbide. *J Am Ceram Soc* 2000;**83**:1548–50.
6. Chiang Y-M, Messner RP, Terwilliger CD, Behrendt DR. Reaction-formed silicon carbide. *Mater Sci Eng* 1991;**A144**:63–74.
7. Zhou H, Singh RN. Kinetics model for the growth of silicon carbide by the reaction of liquid silicon with carbon. *J Am Ceram Soc* 1995;**78**:2456–62.
8. Massalski, TB. (Editor-in-Chief), Murray, JL, Bennett, LH, and Baker, H., ed., *Binary Alloy Phase Diagrams*. American Society for Metals, Metals Park, Ohio, c1986.
9. Fitzer E, Gadow R. Fibre-reinforced silicon carbide. *Am Ceram Soc Bull* 1986;**65**:326–35.
10. Li JG, Hausner H. Reactive wetting in the liquid-silicon/solid–carbon system. *J Am Ceram Soc* 1996;**79**:873–80.
11. Pampuch R, Wasalek E, Bialoskorski J. Reaction mechanism in carbon–liquid silicon systems at elevated temperatures. *Ceram Int* 1986;**12**:99–106.
12. Ness JN, Page TF. Microstructural evolution in reaction-bonded silicon carbide. *J Mater Sci* 1986;**21**:1377–97.
13. Singh M, Behrendt DR. Studies on the reactive melt infiltration of silicon and silicon–molybdenum alloys in porous carbon. In: *NASA Technical Memorandum 105860. Prepared for the 94th Annual Meeting of the American Ceramic Society*. 1992.
14. Favre A, Fuzellier H, Suptil J. An original way to investigate the siliconizing of carbon materials. *Ceram Int* 2003;**29**:235–43.
15. Rudy E. *Ternary Phase Equilibria in Transition Metal–Boron–Carbon–Silicon Systems. Part V. Compendium of Phase Diagram Data, AFML-TR-65-2. Part V*. Ohio: Air Force Materials Laboratory, Metals and Ceramics Division, Wright-Patterson AFB; June 1969.
16. Adelsberg LM, Cadoff LH, Tobin JM. Kinetics of the zirconium–carbon reaction at temperatures above 2000 °C. *Trans Metall Soc AIME* 1966;**236**:972–3.
17. Sara RV. The system zirconium–carbon. *J Am Ceram Soc* 1965;**48**: 243–7.
18. Storm EK. *The Refractory Carbides, A Series of Monographs, vol. 2*. Los Alamos, New Mexico/New York and London: Los Alamos Scientific Laboratory, University of California/Academic Press; 1967. p. 20.
19. Nabarro FRN. The strains produced by precipitation in alloys. In: *Proceeding of the Royal Society, vol. A 18*. 1940. p. 519–38, 175.
20. Porter DA, Easterling KE. *Phase Transformations in Metals and Alloys*. Chapman & Hall; 1992.